Ground ice estimation in permafrost samples using industrial Computed Tomography and Multi-Sensor Core Logging and comparison to destructive measurements

Mahya Roustaei [1,2*], Joel Pumple [1], Jordan Harvey [1], and Duane Froese [1,*]

[1] Department of Earth and Atmospheric Sciences, University of Alberta, Edmonton, Canada

[2] UGent Geotechnical Institute, Ghent University, Technologiepark 68, 9052 Zwijnaarde, Belgium

Correspondence to: Mahya Roustaei (mahya.roustaei@ugent.be) or Duane Froese (duane.froese@ualberta.ca)

Abstract.

Permafrost contains a variety of ground ice types (e.g., pore, segregated, intrusive, vein, or massive ice) that have a diversity of cryotextures which organise to form distinctive cryostructures. The distribution and abundance of those ground ice types determines the potential for thaw subsidence and terrain effects of permafrost landscapes. Analysis of permafrost samples allows improved understanding of ground ice formation, internal and external permafrost processes, and improved tools to predict thaw settlement and consolidation. However, most methods to characterise permafrost are destructive and of low resolution. Here, some of the limitations of traditional destructive methods are overcome using an industrial Computed Tomography scanner (CT). We use this laboratory-based method to systematically characterize five permafrost samples. We visualise cryostructures, measure frozen bulk density, and estimate volumetric and excess ice contents non-destructively and compare these results with traditional destructive analyses at similar spatial scales.

The results show strong agreement between traditional destructive analyses (RMSE's for density, volumetric ice, and excess ice contents are 0.12 g/cm3, 3% and 6%, respectively) as well as recent developments using a Multi-Sensor Core Logger (MSCL) (RMSE's for density and volumetric ice contents are 0.08 g/cm3 and 7%, respectively). These results demonstrate that these non-destructive approaches can produce consistent results, and provide the added benefit of archiving images and enhancing digital permafrost datasets. Development of standardised and interoperable methods for permafrost characterization has the potential to build more robust permafrost datasets and strengthen efforts to understand future thaw trajectories of permafrost landscapes.

1 Introduction

Permafrost is rock or soil that has remained below 0°C for at least two consecutive years. Within permafrost, several different types of ground ice can form: pore ice within the void spaces between soil or rock particles; segregation ice as distinct lenses formed through migration of water within permafrost; aggradational ice, a type of segregation ice, that forms as the permafrost table rises; vein or wedge ice that forms within thermal contraction cracks; intrusive ice that forms when water is injected under pressure; or massive ice that refers to relatively pure bodies of ice within permafrost (Subcommittee on Permafrost., 1988). These differing types of ground ice have distinctive associations of cryotextures, which refer to the appearance and characteristics of ice crystals, gas bubbles and their interfaces with soil particles at a more microscopic scale; and cryostructures which refer to the three-dimensional patterns and arrangements of ice bodies within the frozen ground (such as layered, lenticular, or reticulate patterns) (Murton and French, 1994; French and Shur, 2010). Taken together, these ice-related features help identify the genesis of perennially frozen sediments and can provide insights into the conditions under which the permafrost formed, which can aid in understanding potential ground ice distribution. Of particular importance is excess ice – or ground ice that exceeds the natural pore volume that the sediment would have under unfrozen conditions (Brown et al., 1997; Zhang et al., 1999; Cai et al., 2020; Van Everdingen, 1998). When excess ice melts, it causes thaw settlement and ground subsidence, making its quantification increasingly critical as warming temperatures degrade permafrost across permafrost regions (e.g. Kokelj et al., 2024). Projections of widespread permafrost thaw by the end of this century (e.g. Cai et al., 2020) highlight an urgent need for standardised methods to measure and map excess ice distribution to better predict future landscape changes.

Cryostructural approaches to ground ice classification aim to understand permafrost development by systematically analyzing the shape, size, and spatial patterns of ice inclusions in frozen ground. These methods contrast with more commonly used engineering-focused descriptive systems, which rely primarily on visual descriptions and simple field tests, such as thawing samples to observe supernatant water content. While the descriptive approach provides practical field-based classifications useful for engineering applications, the cryostructural approach offers more process-based insight into permafrost formation processes and potential ground ice distribution, which is increasingly important for predicting thaw settlement and landscape response to climate warming (French and Shur 2010).

Traditional approaches to permafrost characterization rely heavily on visual description of exposures and cores (Kanevskiy et al., 2011; Stephani et al., 2014). While these approaches have advanced our understanding of permafrost, they require substantial experience of the analyst, and are difficult to standardise. Quantitative methods typically require destruction of samples to measure ice and moisture contents, which works well for ice-rich mineral soils but presents challenges for organic-rich materials where water may be retained in thawed samples. These limitations have driven the development of non-destructive methods like Computed Tomography (CT) scanning that can systematically analyse intact frozen cores, providing

standardised, quantitative data on ground ice while preserving samples for additional analyses (Calmels and Allard 2004, 2008, Calmels et al., 2010). This approach offers the potential to better understand permafrost formation, internal structure, and likely response to thaw while developing more consistent and interoperable methods applicable across different permafrost materials.

Micro-computed tomography (μCT), which offers much higher spatial resolution than conventional CT, has emerged as a promising solution to the limitations of traditional permafrost characterization methods since the pioneering work of Calmels and Allard (2004, 2008), who demonstrated its utility for measuring ice and gas contents in permafrost and linking these to processes of ground ice formation. Subsequent studies have expanded the application of μCT scanning to examine cryostructures (Calmels et al., 2010; Fan et al., 2021), excess ice (Lapalme et al., 2017), soil degradation in freeze-thaw cycles (Nguyen et al., 2019; Wang et al., 2018, 2017; Roustaei et al., 2022, Roustaei et al., 2024), quantification of micro-lenticular ice lens formation (Darrow and Lieblappen, 2020), unfrozen water content (Roustaei et al., 2022), soil-ice relations (Torrance et al., 2008), and permafrost composition (Nitzbon et al., 2022).

Although the method has developed, there have been few systematic comparisons of high-resolution μCT scanning (< 100 μm) with established methods for differentiating excess ice from pore ice across different permafrost materials. μCT typically offers very high spatial resolution (down to a few microns) for small samples, while industrial CT provides a balance of higher power and the ability to scan larger samples at slightly lower resolution, and medical CT is generally optimized for human-sized imaging at lower resolution and power. This study addresses this gap by using industrial CT scanning, which offers higher peak power and resolution than medical CT scanners, to analyse five different permafrost cores representing a range of typical properties (e.g., density and ice contents). We develop a new approach using an internal water standard to calibrate linear attenuation coefficients to real density values, and systematically compare CT-derived measurements of frozen bulk density, excess ice, and volumetric ice contents with both destructive physical measurements and Multi-Sensor Core Logging (MSCL).We include a sensitivity analysis to examine how spatial resolution affects excess ice estimation. While our sample set does not capture the full heterogeneity of permafrost materials and ground ice abundance, it provides a rigorous test of CT methods for quantifying ground ice in common permafrost materials.

2 Methods and Materials

2.1 Site and sampling

Five cores were investigated in this study, each representing common materials encountered in permafrost regions, such as silt (ice-poor and ice-rich), peat, silty peat, and diamicton (a coarser, mixed-grain material), and containing a relatively simple vertical cryostratigraphy to minimize the impact of lateral heterogeneity (Table 1). Minimizing lateral heterogeneity is important because such variations can introduce noise when comparing multiple data acquisition methods applied to different, but nearby, sample volumes within the same core (Figure 1). This consideration and its implications are explained further by Pumple et al. (2024), who discuss how variations in measured densities of permafrost cores may reflect real heterogeneities in physical properties or artifacts introduced due to core preparation or mounting of frozen materials.

These cores were collected as during two separate field campaigns in 2013 and 2019 with some cores being collected in southwestern Yukon along the Alaska Hwy and other in Central Yukon along the Dempster Hwy. All cores were collected in a sub-arctic setting. Following extraction, the cores were bagged, labelled and stored at subzero temperatures via a pre chilled cooler and quickly transported to the field base where a chest freezer was present. The chest full of cores was then transported to the Permafrost ArChives Science (PACS) Laboratory and archived into walk-in archive freezer space. Samples were prepared for two different stages; non-destructive scans and destructive physical measurements. As such for the non-destructive scans, physical cores were cut in half and run through all non-destructive data collection methods. For the second stage, a duplicate transect of cuboid samples was collected from the middle of the core to allow non-destructive data analysis at a higher resolution on one set of the subsampled cubes. As seen in Figure 1, this resulted in the cuboids flanking either side of the MSCL and CT results which were collected from a central transect on the half-core samples.

2.2 Industrial Micro Computerised Tomography

Micro Computed tomography (µCT) is a non-destructive technique that has been useful in the investigation of geological porous media (Ashi, 1997; Ketcham and Carlson, 2001; Kozaki et al., 2001; Flisch and Becker, 2007; Calmels and Allard, 2004; Van Geet et al., 2005; Tanaka et al., 2010; Nitzbon et al., 2022). This imaging method captures radiograph images through the production of x-rays which pass through a cabinet and are recorded by the detector panel opposite the source. The sample is placed between the source and the detector panel and the resulting relative absorption of the x-rays energy is recorded by the detector panel creating the radiograph image. To collect a 3 dimensional image, a set of two-dimensional X-ray radiographs are collected at multiple angles, and secondly reconstructed to form a 3D image. The final measurement unit, commonly visualized as a histogram, is the linear attenuation coefficient, which depends on both the density and the electron density of the material (Ketcham and Carlson, 2001).

The scans presented here were captured using a helical scan with a Nikon XTH 225 ST cabinet-based industrial computed tomography micro-CT scanner. The system uses an electronically adjustable 225Kv 225W power source (Figure

2). This system includes both a tungsten rotating reflection target source and a tungsten fixed reflection target source coupled with a 16-bit 2000x2000 pixel detector capable of a focal spot size range of 3-121 μm depending on the size of the area of interest and size of the object being scanned. The 10 cm diameter frozen permafrost half cores were scanned with the reflection target source at 200 Kv 35 μa with an exposure time of 125 ms and a voxel (3D volume element representing pixel resolution and slice thickness) size of 65 μm. Scan times ranged from 30 to 45 minutes per core, with a maximum height of ~12 cm scanned per core due to vertical stage movement limitations and inclusion of calibration materials. The subsampled cubes from the cores were scanned with the rotating reflection target source at 225 Kv 133 μa with an exposure time of 125 ms and a voxel size of 25 μm. Scan times for the subsampled cubes were 30 minutes per cuboid. The images were reconstructed into three-dimensional grey-scale volumes using the Nikon CT pro 3D software and analyzed using ORS Dragonfly 2022 image processing software (ORS 2021).

An insulated sample holder was developed for this project to ensure samples remained frozen during CT scanning. Both cubes and cores were housed in the same style of a styrofoam container, however, the internal setup varied due to the size of the sample under investigation. Full cores were taken from a nearby chest freezer and placed vertically into a larger container (12 cm inner diameter), with a -80 °C ice pack positioned directly above (Figure 2B and C). In contrast, the cubes were placed in smaller containers (9 cm inner diameter), held in plastic vials beneath a foam divider, and cooled with dry ice on a perforated foam layer to circulate cold air over the sample (Figure 2D). These configurations were tested in advance using internal, surface, and air temperature probes, confirming that both setups maintained sub-zero temperatures for the full scan duration. It should also be noted that full core scans produced partial results due to vertical stage height limitations in the CT scanner. While the scanner can hold samples up to ~30 cm wide by 35 cm high, the maximum scan height depends on voxel resolution and sample width. This limitation was resolved once the cores were subsampled for destructive testing. As a result, for some cores, such as the peat core, it was not possible to compare full vertical data sets across MSCL, CT, and destructive methods.

2.2.1 CT Calibration

The linear attenuation coefficient (μ) represents the energy attenuated within a single voxel volume while the voxel population is the population of voxels within a scan volume (Ketcham & Carlson, 2001). By creating a histogram (linear attenuation coefficient vs voxel population) with these values, distributions of relative grey values can be presented. If uncalibrated, the resulting grey values observed in the histogram of a CT scan appear as linear attenuation coefficients. The medical field has developed methods for converting linear attenuation coefficients to Hounsfield units and as a result, the Hounsfield unit has become commonly used in CT research (Hounsfield, 1973; Wellington and Vinegar, 1987; Duliu, 1999; Knoll, 2000; Ketcham and Carlson, 2001; Duchesne et al., 2009). Lee et al., 2015 took it one step further and converted mean Hounsfield unit values to bone mineral density values (mg/cm^3) via a linear regression analysis. A similar approach was used in this study by collecting the CT scans with an internal standard of known density (water) later used to calibrate the resulting linear attenuation

148 coefficients into g/cm³ using the Nikon CT Pro 3D software (CT Pro version 5.4). It should be noted that all cores were scanned
149 with ice, water, and aluminum calibration pieces of which water proved to be in closest agreement with destructive analyses.
150 The water and aluminum were located outside of the insulated container during the core scans to avoid freezing. The cube
151 scans had only the water located directly above the cube sample but isolated from the sample and dry ice by insulated foam to
152 minimize the exposure to the cold air temperature within the developed insulated container. The aluminum calibration piece
153 generally underestimated the bulk density while the ice calibration piece resulted in a slight overestimation. Aluminum was
154 chosen for its consistent density of 2.71 g/cm³ representing an upper limit of the expected bulk density within the selected
155 materials. The ice calibration was a 15 ml falcon tube filled and frozen at -5C to minimize expansion issues and bubbles.
156 Overall the water calibration produced the most accurate results apart from ice-poor sediments. The Nikon CT Pro 3D software
157 uses a linear two-point calibration with the first fixed point being air (equal to zero) and the second a user-defined value based
158 on a user-selected pixel population. A representative (local) population of pixels was selected from our water sample in a 2D
159 slice of the scan and informed the expected average target value (1 g/cm³). This results in displaying grey values in g/cm³.
160 These densities can then be presented in a histogram, the shape of which reflects the volumetric content of the components in
161 the sample (Calmels et al. 2010).

162 **2.2.2 Image Processing**

163 Image preprocessing usually consists of two main stages; 1) selection of the Region of Interest or (ROI), 2) segmentation. In
164 this study both stages were done using Dragonfly software (ORS 2021). This software enabled us to process the three-
165 dimensional reconstructed X-ray tomographs of the frozen materials to segment, quantify, calculate, and illustrate the cores'
166 physical properties. For the first stage, a series of ROIs were created in the half core CT results down the central vertical axis
167 of the cores to mimic the data collection points of the MSCL as presented in Pumple et al. (2024). Figure 1 displays the relative
168 location of these ROIs which were sized to match the spot size of the gamma-ray at the surface of the core, ~10 mm in diameter.
169 The central point of each ROI was placed 5 mm apart resulting in a significant overlap between adjacent data points, again
170 similar to the data collection process for the MSCL. In this study, all cores were calibrated so the histogram values were
171 displayed in g/cm³. Following calibration, the histograms served not only as visualization tools but also as a means to extract
172 quantitative information. To extract the frozen bulk density from each ROI, the mean grey values were extracted in calibrated
173 density values (g/cm³).
174 The second stage, segmentation or the ability to differentiate materials, depends on their respective linear attenuation
175 coefficients, meaning materials with divergent densities and/or atomic numbers are easier to differentiate (Kyle and Ketcham,
176 2015). Analysing a multi-modal histogram of a CT image is straightforward for material differentiation while materials with
177 similar unimodal density distributions may appear as a single peak in the histogram (Wang et al., 2024). In addition to the
178 relative density of the scanned materials, the image resolution or voxel size also directly impacts the image segmentation
179 process. The voxel size can impact the image segmentation through the partial volume effect which relates directly to the

resolution or voxel size of the scan and for geological samples, to grain size, minimal pore size, and organic content (Soret et al., 2007; Nitzbon et al., 2022).

In this study, an automatic image thresholding method named "Otsu " was used. The algorithm of this method, proposed by Nobuyuki Otsu (1979), performs automatic clustering-based image thresholding, assuming that there are two classes of pixels which are "*foreground*" and "*background*" pixels of the image. The optimum thresholding is calculated by distinguishing the two classes so that the minimum class variance is obtained (Kumar and Tiwari, 2019). This method was applied to the selected regions of interest from stage one to differentiate sediment and ice. In each image processing step, we tried to isolate the materials within our scans based on density and slowly slice away the lighter density portion (ice) until we are certain we have collected the target material range (often a mixture of ice and sediment). Figure 3 shows the ice (less dense material) being segmented from the surrounding sediment through multiple image processing steps using the Otsu method where only the background (less dense) portion of the previous step is added to the final result. This approach shows that applying the first image processing step will mainly extract the visible ice while using multiple Otsu analyses additional lower-density ice-rich mixtures (mainly pore ice) are extracted, e.g., the area shown inside the red circle of Figure 3B-D. Note that all the above mentioned segmentation steps can also be done by visual inspections instead of automatic thresholding method but it can vary significantly between users, leading to inconsistent results.

2.3 Physical Density Measurements

Ground-ice content is typically expressed either as the *gravimetric moisture/ice content* (the ratio of the mass of the ice in a sample to the mass of the dry sample) or the *volumetric moisture/ice content* (the ratio of the volume of ice in a sample to the volume of the whole sample) (Van Everdingen, 1998). Excess ice refers to the amount of ice in the soil that exceeds the volume of the pore space in the unfrozen state (Subcommittee on Permafrost., 1988). Similar to thaw-strain measurements in geotechnical investigations (Crory, 1973; Shur, 1988; Pullman et al., 2007; Kanevskiy et al., 2012), Kokelj and Burn (2003) and O'Neill and Burn (2012) both applied a method for destructively extracting excess ice content measurements from frozen samples. This method includes the complete thaw, homogenization, and settling time of the sample to extract the supernatant water content and estimate excess ice content. Their method does not require measurement of frozen sample volume since the volumes of sediment as well as the supernatant water should be recorded from the graduated beakers containing the samples once completely thawed. The excess ice content (E_i) of the samples can then be estimated by the equation (Kokelj and Burn, 2003):

$$(Ei) = \frac{(Wv*1.09)}{(Sv+Wv*1.09)} * 100 \tag{1}$$

where Wv is the volume of supernatant water (cm^3), multiplied by 1.09 to estimate the equivalent volume of ice, and Sv is the volume of saturated sediment (cm^3).

This study takes an approach similar to Kokelj and Burn (2003) in that the supernatant moisture content is destructively assessed in order to calculate excess ice content. However, since the volume of soil samples was precisely measured through the following steps (Pumple et. al, 2024), volumetric ice contents were also measured.

To independently assess density and ice content measurements and also being able to perform scans at higher resolutions, the cores were subsampled as 2x2x4cm cubes. The subsampling process was done in a walk-in freezer maintained at −7°C. The initial step involved removing material from the outer edges of the whole core that might have thawed during coring or been affected by sample storage. Core segments were split lengthwise with a rock saw equipped with a 35 cm diameter diamond-cutting wheel. Cuboid aliquots were cut from one half of the split core, while the other half was retained as an archive. The rounded edges were removed from the half core to expose an internal slab. For this study, a duplicate set of cuboids was obtained by cutting the internal slab in half. Approximately 3 cm³ aliquots were subsampled from the cores for samples with low ice contents to ensure that the cuboids did not fracture or disintegrate during sampling. Digital callipers (±0.01 mm) and a digital analytical balance (±0.01 g precision) were used to measure physical dimensions and mass, respectively, to calculate the frozen bulk density. The cuboids were then thawed at room temperature for 24 hours in glass beakers covered with Parafilm to minimize evaporative loss. Excess moisture was removed from the beakers containing the thawed samples, and the sample weight was recorded again to calculate excess moisture content. The cuboids were then dried in an oven for 24 hours at 105°C and reweighed to determine both volumetric ice content and gravimetric moisture content. Finally, the remaining dried material was heated at 550°C for 4 hours to determine the percent organic content via loss on ignition. High organic content could result in water absorption by soil matrix upon thaw and more complexity in the measurements of excess ice contents.

Because in some soils, such as peat, excess ice will be absorbed by the soil skeleton upon thaw (Johnston, 1981), the Kokelj and Burn method was adjusted for samples with high organic contents by applying a slight pressure on the thawed cube and extraction of the released water. Additionally, the organic content of each sample was measured via loss on ignition (LOI) (Heiri et al., 2001). The *cuboid* method, described by Bandara et al. (2019), is similar to other volumetric and gravimetric methods used to measure bulk density and ice content, but takes advantage of the frozen state of the material which allows for a greater accuracy of volume measurement. Processing is undertaken in a walk-in freezer following methods outlined in Pumple et al. (2024).

2.4 Multi Sensor Core Logger (MSCL)

The PACS Laboratory MSCL is a floor-mounted, automated logging system, manufactured by Geotek, which can be used to analyse whole or split cores. This core logger is equipped with two magnetic susceptibility instruments, a line-scan camera, and a Caesium-137 (^{137}Cs) gamma source and detector which provides measurements of gamma attenuation. Pumple et al. (2024) provides additional details on the methods used for the MSCL data collection and calibration. This analysis yields key physical parameters such as frozen bulk density and volumetric ice content, derived from gamma attenuation measurements

243 combined with soil density estimates and established equations (Lin et al., 2020). We used the density and volumetric ice

244 content results reported by Pumple et al. (2024) as an established non-destructive reference technique to validate and compare

245 with our own ice content estimations.

246

3 Results and Discussions

248   Figures 4 A and B show one slice of a small ROI and its histogram from 5 different cores of this study. The differences

249 in the shapes of the histograms are due to the different sediment densities. The diamicton core has the highest sediment density

250 and a bimodal histogram in which the first mode represents ice and the second is related to the sediments and clasts. Whereas

251 in the other cores, ice and sediment appear as a single mode. Image segmentation of these slices using the Otsu method resulted

252 in the differentiation of 5 different classes of ice/sediment ratios on the basis of their relative densities; air, low ice or sediment-

253 poor ice, high ice or sediment-rich ice, low sediment or ice-rich sediments, and high sediment or ice-poor sediments or clasts

254 shown in Figures 4 B and C. Low ice comprises primary visual or excess ice; high ice mainly results from extraction of pore

255 ice or ice proximal to sediment (sediment-rich ice). It should be noted that the pore ice inclusions within the mineral soil matrix

256 are often smaller than the spatial resolution of the CT and the resulting grey value of a voxel is related to the mixture

257 composition of low-density ice and high-density mineral grains. This phenomenon, called partial volume effect, is the main

258 reason why the high ice appears denser. Low sediment and high sediment categories differentiate ice-rich sediments from

259 sediments with lower and higher densities, respectively. Figure 5a-f illustrate the image segmentation results for the whole

260 diamicton core, highlighting these distinctions.

261

3.1 Core Results

263

3.1.1 Ice-rich Silt Core (BH18-211):

265 Figure 6 shows the destructive (cuboid) and non-destructive (CT and MSCL) results of the ice-rich silt core, illustrating that

266 the CT frozen bulk densities are in strong agreement with both the cuboid (RMSE = 0.12 g/cm^3) and MSCL (RMSE = 0.14

267 g/cm^3) results. This core has a high organic content (8-19% organic), micro-lenticular and layered cryostructures, and 66%

268 silt. Cuboid physical EIC and VIC measurements range from 19-34% and 68-76%, respectively, while the CT EIC and VIC

269 estimates range from 20-68% and 32-74% at the same depths where cuboid measurements were collected. The 65 μm EIC

270 (redline in Figure 6C) shows good accordance with the cuboid EICs (RMSE = 9%) apart from the ice layer where the cuboid's

271 relatively low sample resolution results in an averaging out of the ice content across the ice layer. The 65 μm CT-VICs (black

272 line in Figure 6C) illustrate the resolution limitation in extracting the pore ice of this sandy silt core while the 25μm VICs

273 shown as black cubes in the same plot tackle this limitation and agree well with VICs extracted from the Cuboid method

274 (RMSE = 7%). The MSCL VICs follow the same trend as the cuboid data (Fig 6-C) but consistently tend toward lower values

275 in the ice-poor regions.

3.1.2 Transition Core (BH12F-138):

277 Figure 7 shows the results of the transition core from both destructive (cuboid) and non-destructive (CT and MSCL) methods,

278 illustrating a sharp boundary between an ice-rich silty peat, containing massive and rare crustal cryostructures, and an ice-poor

279 inorganic silt with a mainly micro-lenticular cryostructure. The organic content of the core's top section, ranging from 53-

280 71%, highlights this transition (Figure 7D). Cuboid physical EIC and VIC measurements range from 6-28% and 64-88%,

281 respectively, while the CT EIC and VIC estimates range from 9-33% and 42-95% at the same depths where cuboid

282 measurements were collected. This figure also shows that the CT bulk density results are in strong agreement with both the

283 cuboid (RMSE = 0.13 g/cm^3) and gamma attenuation data (RMSE = 0.06 g/cm^3) in agreement with the results reported by

284 Pumple et al., 2024. The 65 μm EIC results (red line in Figure 7-C) follow the cuboid results (RMSE = 5%) in the silty section.

285 The 65 μm VIC (black line in Figure 7C) resolves more than 50% of pore ice, while the higher resolution (25 μm, black cubes

286 in Figure 7C), estimates up to 100% (RMSE = 3%).

3.1.3 Diamicton Core (BS19-3-6):

288 Figure 8 illustrates the destructive (cuboid) and non-destructive (CT and MSCL) results of the diamicton core. This ice-rich

289 diamicton contains both suspended and crustal cryostructures and more than 50% silt (Table 1). Overall the bulk density and

290 ice measurements from CT display high concordance with the gamma attenuation (RMSE = 0.14 g/cm^3), and cuboid (RMSE

291 = 0.14 g/cm^3) methods (Figure 8). Cuboid physical EIC and VIC measurements range from 30-50% and 48-66%, respectively,

292 while the CT EIC and VIC estimates range from 22-57% and 36-77% at the same depths as the cuboid measurements. The 65

293 μm EIC results (red line in Figure 8C) follow the cuboid results (RMSE = 8%). The only point where the datasets differ notably

294 is at 2-4 cm depth where the MSCL values shifts towards lower densities due to the core's lateral heterogeneity while the CT

295 density still lines up well with the cuboid results. The ice contents of this cube are also much lower than CT and MSCL results.

296 This is due to the collection procedure of the cubes which were just off-center to accommodate a duplicate run of cubes down

297 the middle of the core for CT imaging and destructive measurements (as shown in Figure 1). This single cube highlights the

298 effect of differences in the locations of ROIs between CT/MSCL and the cuboid methods. Moreover, at this depth in the core

299 cuboid sample, there was a clast which resulted in a local density high and lower ice content.

300 In this core, the 65 μm VICs agree well with the cuboid-VICs, MSCL (RMSE = 4%) ice contents, and 25 μm cube

301 scan results (RMSE = 3%) while in the transition core, the 65 μm VICs underestimated the other VIC results. The difference

302 between the 65 um VIC results and other VIC results for all cores except the diamict could be a result of the sample's grain

303 size as the diamict has high clay content (~18%) relative to the other cores (~8-12%) (Table 1).

3.1.4 Ice-poor Silt Core (BH20B-337):

Figure 9 shows the results of the ice-poor silt core from both destructive (cuboid) and non-destructive (CT and MSCL) methods, illustrating a massive (non-visible) cryostructure within this inorganic silt that highlights the relatively low overall ice content throughout the core. This core has little variability throughout its profile. The CT bulk densities are consistent with both the cuboid (RMSE = 0.14 g/cm^3) and gamma attenuation data (RMSE = 0.14 g/cm^3). The 65 μm EIC results compare well with the cuboid EIC results (RMSE = 5%) while the 25 μm cube scan ice contents show strong agreement (RMSE = 3%) with the volumetric cuboid ice content estimates. It should be noted that based on the EIC results of 65 μm scans, the core has a small percentage of ice (around 5%) in the form of microstructures beyond the natural pore space within the host sediment. However, upon thawing, the surrounding sediment absorbs the moisture into the available pore space, resulting in no EIC during the destructive analysis.

3.1.5 Peat Core (DH13-589):

Figure 10 illustrates the destructive (cuboid) and non-destructive (CT and MSCL) characterization results of the peat core, with little variability throughout its profile. The core is formed of homogenous organics, with an organic-matrix cryostructure of visible ice within the densely packed peat. The CT bulk density results are similar to both the cuboid (RMSE = 0.05 g/cm^3) and gamma attenuation results (RMSE = 0.03 g/cm^3) (Figure 10). The 65 μm ice content results (39-48% of EIC) are also in accordance with the cuboid excess ice results (RMSE = 4%). The 65 μum and 25 μum VICs are both showing good estimates of VICs (RMSE = 1%). It should be considered that the adjusted method for extraction of supernatant water, using slight pressure to release water from the organic matrix, was applied to the cubes of this core. As it was previously discussed, this pressure will release the excess water that was absorbed by the peat skeleton upon thaw (Johnston, 1981).

3.2 Sensitivity analysis

In this study in order to do a sensitivity analysis and investigate the impact of resolution on the delineation between ice and sediment, repeat scans were conducted on the same cube. Initially, the half cores (10 cm diameter) were scanned with a 65 μm voxel size. This was due to the physical size (width) of the imaging window. The smaller size of the cubes, however, presented an opportunity to collect data from the same material but at a resolution of 25 μm. Some of the cubes were also scanned at the same 65 μm resolution as the half cores to make a direct comparison. Figure 11 shows the same slice location and orientation from the same cube at two different resolutions.

A ROI, shown as a red square in Figure 11, was then selected in each CT-scanned cube to make a direct comparison between the delineated (Otsu split) ice contents from image processing and the ice contents determined from the destructive cuboid analysis of the corresponding cube sample. As reference points, the cuboid ice content results for this cube were as follows; 22% excess ice and 65% volumetric ice contents. Figure 12 shows the collected data from repeat image processing steps using the Otsu method of each cube scanned at both 25 μm and 65 μm resolutions as well as the cuboid results. The initial

335 image processing steps for both the 25 μm and 65 μm scans closely capture the expected value of the EIC. However, only the
336 25 μm cube captures a representative value relative to the cuboid data for the measured volumetric ice content. This value is
337 reached after 6 image processing steps using the Otsu method. These results illustrate the capability of 25 μm resolution for
338 better extracting trapped ice inside pore spaces of this sandy silt sample which could be due to the smaller size of pores than
339 the resolution. The nature of the curve suggests that VIC cannot be delineated from the 65 μm resolution scans however EIC
340 is possible.

341 Additionally, there is an observable increase in the amount of pore space or gas captured in the 25um resolution
342 relative to the 65um. This difference highlights the 25um scan's increased potential to capture, and as a result segment, the
343 different components within the scanned material.

3.3 Comparison of CT and Cuboid Density and Excess Ice Results:

345 Segmentation of the CT images using the Otsu method allows comparison of CT-derived bulk densities, excess ice, and
346 volumetric ice contents with estimates from the cuboid method at similar resolution. We completed these comparisons at 65
347 μm and 25 μm (Figures 13, 14 and 15). These figures revealing a good agreement for density, excess ice, and volumetric ice
348 measurements with RMSE of 0.12 g/cm^3, 6%, and 3%, respectively. Additionally, the CT results compare well with the MSCL
349 results for both density and VIC with RMSE's of 0.08 g/cm^3 and 7%, respectively (Figures 16 and 17). The differences between
350 the estimated EICs from CT image processing (65 μm-whole core) and the measured ones from the cuboid method are due to
351 the differing resolutions, i.e., 0.5 cm for CT and 2 cm for the cuboid method, as well as the different locations of the regions
352 of interest (previously described in section 2.2). The strong accordance of the VICs highlights the opportunity for higher
353 resolution scans to estimate pore ice.

3.4 Comparison of Non-destructive Methods:

355 The results of this study show strong agreement between the two non-destructive methods: CT and MSCL and highlight the
356 importance of continued development and refinement of non-destructive methods for extracting physical properties from
357 permafrost materials.

358 The presented CT method allows for whole core high-resolution (65 μm) three-dimensional imaging of cores,
359 measurement of bulk density and estimation of excess ice contents at a desired scale. This contrasts with MSCL which is
360 restricted to a fixed data collection transect down the center of the core (~ 1cm wide) with a maximum sample resolution of ~
361 0.5 cm, high resolution (25 μm) 2-dimensional half-core images and currently provides only volumetric ice estimates, and no
362 direct estimates of excess ice. The CT method is capable of estimating volumetric ice contents but requires cores to be
363 subsampled to a smaller size (2x2x4 cm cube) to allow for finer resolution scans (25 μm).

364 It is worth noting that the MSCL provides a more rapid method for collecting bulk density and volumetric ice content
365 estimations in comparison with the CT method. However, in addition to bulk density and volumetric ice content estimations,

the CT method can provide direct estimates of excess ice content. Visible ice can be segmented and isolated from the remaining sediment and pore ice when scanning split cores at 65 μm voxel size, allowing the opportunity to better estimate EIC values compared to MSCL methods. Therefore, in terms of a non-destructive method for identifying and quantifying excess ice within permafrost cores the CT method provides a more robust approach although the image processing and acquisition costs are significantly greater.

4 Conclusions

This study investigated the application of high-resolution industrial CT scanning as a non-destructive method to tackle the limitations of traditional destructive methods (e.g., visual acuity, poor reproducibility, and low resolution) in permafrost characterization. Investigations were done by systematically logging permafrost cores, visualising cryostructures, measuring bulk density, and estimating volumetric and excess ice contents, independently. Five permafrost cores, representing common materials encountered in permafrost regions, were scanned at voxel sizes of 65 and 25 μm. A new calibration method was used to extract real densities in g/cm^3 directly from CT images. Image segmentation results using Otsu automatic image thresholding method illustrated the effectiveness of this method in generating robust segmentation results while the visual inspection method has its own drawbacks, e.g. inspector's visual acuity and poor reproducibility.

The initial identification of different materials from CT images showed 3 classes; air (gas), ice, and sediments while image processing steps of the scans (using Otsu method) illustrated significant density differences in ice and sediment classes. Image segmentation results using multiple image processing steps showed visual/excess ice as a lower density relative to the pore ice and delineated two sediment classes based on densities.

Since manual and visual thresholding is subject to operator experience and judgement and also not applicable in images with unimodal histograms related to materials with close densities (organic materials and ice), an automatic thresholding technique was used in this study to generate more consistent results.

Comparison of the image processing results and extracted physical properties of 5 permafrost cores were validated against a destructive method (cuboid) and MSCL non-destructive method. The results showed strong agreement between these three methods (CT and cuboid) considering their differing resolutions and regions of interest with overall average RMSE's of 3%, 6% and 0.12 g/cm^3 for VIC, EIC and density, respectively. This agreement demonstrates the applicability and reliability of non-destructive methods in tracking physical and cryostructural details of permafrost cores and producing replicable, cost-effective measurements. A sensitivity analysis of the impact of differing resolutions on the delineation between ice and sediment showed that higher resolution scans generate more accurate VICs while the lower resolution scans are still sufficient for estimation of EICs and a rough estimation of VICs.

The proposed approach of this study will help build more robust permafrost datasets and strengthen future permafrost research efforts in mapping permafrost properties and the distribution of excess ice and predicting thaw settlement. It also presents an opportunity to develop methods to extract more information from existing datasets based on an acute understanding

399 of the relations between key physical permafrost properties. The next steps can be followed by improving our understanding
400 and techniques of scanning permafrost as well as using machine-learning-based image segmentation methods to generate
401 datasets and explore the relations between physical permafrost properties.

Author contribution

403 MR, JP, DF, and JH planned the project; MR, JH, and JP developed the methods; MR, JH, and JP performed the measurements;
404 MR and JH analyzed the data; MR, JP and JH wrote the manuscript draft; MR, JP, JH, and DF reviewed and edited the
405 manuscript.

Competing interests

407 The authors declare that they have no conflict of interest.

Acknowledgements

409 The authors would like to thank Evan Francis who helped with sample preparation in earlier experiments. We would also like
410 to thank Nikon Metrology for the support and constructive feedback they provided throughout the project. Casey Buchanan is
411 thanked for collecting the diamict sample used in this study.

Financial support

413 This research was supported by the NSERC funded Permafrost Partnership Network for Canada (PermafrostNet) and NSERC
414 Discovery grant to Duane Froese. Laboratory infrastructure for the Permafrost Archives Laboratory was funded by Canadian
415 Foundation for Innovation, Government of Alberta, and University of Alberta.

References

417 Ashi, J., Computed tomography scan image analysis of sediments, in Proc. ODP, Sci. Results, edited by Shipley, T. H., Y.
418 Ogawa, P. Blum, and J. M. Bahr, 156, 151–159, 1997.
419 Bandara, S., Froese, D. G., St. Louis, V. L., Cooke, C. A., and Calmels, F.: Postdepositional Mercury Mobility in a Permafrost
420 Peatland from Central Yukon, Canada, ACS Earth Sp. Chem., 3, 770–778,
421 https://doi.org/10.1021/acsearthspacechem.9b00010, 2019.

Brown, J., Ferrians, O., Heginbottom, J., and Melnikov, E. S.: Circum-Arctic map of permafrost and ground-ice conditions, https://doi.org/10.3133/cp45, 1997.

Cai, L., Lee, H., Schanke Aas, K., and Westermann, S.: Projecting circum-Arctic excess-ground-ice melt with a sub-grid representation in the Community Land Model, Cryosphere, 14, 4611–4626, https://doi.org/10.5194/tc-14-4611-2020, 2020.

Calmels, F. and Allard, M.: Ice segregation and gas distribution in permafrost using tomodensitometric analysis, Permafr. Periglac. Process., 15, 367–378, https://doi.org/10.1002/ppp.508, 2004.

Calmels, F. and Allard, M.: Segregated ice structures in various heaved permafrost landforms through CT Scan, Earth Surf. Process. Landforms, 33, 209–225, https://doi.org/10.1002/esp.1538, 2008.

Calmels, F., Clavano, W. R., and Froese, D. G.: Progress on X-ray computed tomography (CT) scanning in permfrost studies, in: GeoCalgary 2010 : the 63. Canadian geotechnical conference and 6. Canadian permafrost conference, Calgary, AB (Canada), 12-15 Sep , 1353–1358, 2010.

CT Pro version 5.4, Nikon Metrology, Brighton, MI, USA

Crory, F.: Settlement associated with the thawing of permafrost, Hanover, New Hampshire, 599–607 pp., 1973.

Darrow, M. M. and Lieblappen, R. M.: Visualizing cation treatment effects on frozen clay soils through μCT scanning, Cold Reg. Sci. Technol., 175, https://doi.org/10.1016/j.coldregions.2020.103085, 2020.

Duchesne, M. J., Moore, F., Long, B. F., , Labrie, J.: A rapid method for converting medical Computed Tomography scanner topogram attenuation scale to Hounsfield Unit scale and to obtain relative density values. Engineering Geology 103, 100–105, 2009.

Duliu, O.: Computer axial tomography in geosciences: an overview. Earth-Sci. Rev. 48 (4), 265–281, 1999. https://doi.org/10.1016/S0012-8252(99)00056-2

Van Everdingen, R. O.: MULTI-LANGUAGE GLOSSARY of PERMAFROST and RELATED GROUND-ICE TERMS, Calgary, 1998.

Fan, X., Lin, Z., Gao, Z., Meng, X., Niu, F., Luo, J., Yin, G., Zhou, F., Lan, A.: Cryostructures and ground ice content in ice-rich permafrost area of the Qinghai-Tibet Plateau with Computed Tomography Scanning. Journal of Mountain Science. 18. 1208-1221. 10.1007/s11629-020-6197-x, 2021.

French, H. M.: The Periglacial Environment, Wiley, 2007, https://doi.org/10.1002/9781118684931

Flisch, A., and Becker, A.: Industrial X-ray computed tomography studies of lake sediment drill cores. In: Mees, F., Swennen, R., Van Geet, M., Jacobs, P. (Eds.), Applications of X-ray Computed Tomography. Geological Society, London, Special Publication, 215, pp. 205–212, 2003. https://doi.org/10.1144/GSL.SP.2003.215.01.19

French, H., & Shur, Y.: The principles of cryostratigraphy. Earth-Science Reviews, 101(3-4), 190-206, 2010. https://doi.org/10.1016/j.earscirev.2010.04.002

453 Heiri, O., Lotter, A.F. and Lemcke, G., 2001. Loss on ignition as a method for estimating organic and carbonate content in
454 sediments: reproducibility and comparability of results. Journal of paleolimnology, 25(1), pp.101-110.
455 https://doi.org/10.1023/A:1008119611481.

456 Hounsfield, G.N.: Computerized transverse axial scanning (tomography). Part I. Description of system. Br. J. Radiol. 46 (552),
457 1016–1022, 1973. https://doi.org/10.1259/0007-1285-46-552-1016

458 Johnston, G. H.: Permafrost: engineering design and construction, National Research Council Canada. Associate Committee
459 on Geotechnical Research, 1981.

460 Kanevskiy, M., Shur, Y., Fortier, D., Jorgenson, M.T., Stephani, E., 2011a. Cryostratigraphy of late Pleistocene syngenetic
461 permafrost (yedoma) in northern Alaska, Itkillik River exposure. Quaternary Research 75, 584–596
462 http://dx.doi.org/10.1016/j.yqres.2010. 12.003, 2011.

463 Kanevskiy, M., Shur, Y. L., Connor, B., and Dillon, M. R.: Study of the Ice-Rich Syngenetic Permafrost for Road Design
464 (Interior Alaska), in: Tenth International Conference on Permafrost TICOP, 191–196, 2012.

465 Ketcham, R. A. and Carlson, W. D.: Acquisition, optimization and interpretation of X-ray computed tomographic imagery:
466 applications to the geosciences, Comput. Geosci., 27, 381–400, https://doi.org/10.1016/S0098-3004(00)00116-3, 2001.

467 Kokelj, S. V. and Burn, C. R.: Ground ice and soluble cations in near-surface permafrost, Inuvik, Northwest Territories,
468 Canada, Permafr. Periglac. Process., 14, 275–289, https://doi.org/10.1002/ppp.458, 2003.

469 Kokelj, S. V. and Jorgenson, M. T.: Advances in Thermokarst Research, Permafr. Periglac. Process., 24, 108–119,
470 https://doi.org/10.1002/ppp.1779, 2013.

471 Kozaki, T., Suzuki, S., Kozai, N., Sato, S., and Ohashi, H.: Observation of Microstructures of Compacted Bentonite by
472 Microfocus X-Ray Computerized Tomography (Micro-CT), J. Nucl. Sci. Technol., 38, 697–699,
473 https://doi.org/10.1080/18811248.2001.9715085, 2001.

474 Knoll, G.F.: Radiation Detection and Measurement. John Wiley and Sons, New York, 1999.

475 Kumar and Tiwari: A Comparative Study of Otsu Thresholding and K-means Algorithm of Image Segmentation, Int. J. Eng.
476 Tech. Res. , 9, 2019.

477 Kyle, J. R. and Ketcham, R. A.: Application of high resolution X-ray computed tomography to mineral deposit origin,
478 evaluation, and processing, Ore Geol. Rev., 65, 821–839, https://doi.org/10.1016/j.oregeorev.2014.09.034, 2015.

479 Lapalme, C. M., Lacelle, D., Pollard, W., Fortier, D., Davila, A., and McKay, C. P.: Cryostratigraphy and the Sublimation
480 Unconformity in Permafrost from an Ultraxerous Environment, University Valley, McMurdo Dry Valleys of Antarctica,
481 Permafr. Periglac. Process., 28, 649–662, https://doi.org/10.1002/ppp.1948, 2017.

482 Lin, Z., Gao, Z., Fan, X., Niu, F., Luo, J., Yin, G., and Liu, M.: Factors controlling near surface ground-ice characteristics in
483 a region of warm permafrost, Beiluhe Basin, Qinghai-Tibet Plateau, Geoderma, 376, 114540,
484 https://doi.org/10.1016/j.geoderma.2020.114540, 2020.

Murton, J. B., & French, H. M.: Cryostructures in permafrost, Tuktoyaktuk coastlands, western arctic Canada. Canadian Journal of Earth Sciences, 31(4), 737-747. DOI:10.1139/e94-067, 1994.

Nguyen, T. T. H., Cui, Y.-J., Ferber, V., Herrier, G., Ozturk, T., Plier, F., Puiatti, D., Salager, S., and Tang, A. M.: Effect of freeze-thaw cycles on mechanical strength of lime-treated fine-grained soils, Transp. Geotech., 21, 100281, https://doi.org/10.1016/j.trgeo.2019.100281, 2019.

Nitzbon, J., Westermann, S., Langer, M., Martin, L. C. P., Strauss, J., Laboor, S., and Boike, J.: Fast response of cold ice-rich permafrost in northeast Siberia to a warming climate, Nat. Commun., 11, 2201, https://doi.org/10.1038/s41467-020-15725-8, 2020.

Nitzbon, J., Gadylyaev, D., Schlüter, S., Köhne, J. M., Grosse, G., & Boike, J. (2022). Brief communication: Unravelling the composition and microstructure of a permafrost core using X-ray computed tomography. The Cryosphere, 16, 3507–3515. https://doi.org/10.5194/tc-16-3507-2022

O'Neill, H. B. and Burn, C. R.: Physical and temporal factors controlling the development of near-surface ground ice at Illisarvik, Western Arctic coast, Canada, Can. J. Earth Sci., 49, 1096–1110, https://doi.org/10.1139/E2012-043, 2012.

Object Research Systems. Dragonfly; Object Research Systems: Montreal, QC, Canada, 2021.

Otsu, N.: A Threshold Selection Method from Gray-Level Histograms, IEEE Trans. Syst. Man. Cybern., 9, 62–66, https://doi.org/10.1109/TSMC.1979.4310076, 1979.

Pumple, J., Monteath, A., Harvey, J., Roustaei, M., Alvarez, A., Buchanan, C., & Froese, D. (2024). Non-destructive multi-sensor core logging allows rapid imaging, measurement of bulk density and estimation of ice content in permafrost cores. *EGUsphere*,18,, 489-503. https://doi.org/10.5194/tc-18-489-2024

Pullman, E. R., Jorgenson, M. T., and Shur, Y.: Thaw settlement in soils of the Arctic Coastal Plain, Alaska, Arctic, Antarct. Alp. Res., 39, 468–476, https://doi.org/10.1657/1523-0430(05-045)[PULLMAN]2.0.CO;2, 2007.

Roustaei, M., Pumple, J., Harvey, J., and Froese, D.: Estimating ice and unfrozen water in permafrost samples using industrial computed tomography scanning, in: GeoCalgary 2022, 2022a.

Roustaei, M., Pumple, J., Hendry, M. T., Palat, A., and Froese, D.: Freeze-thaw impacts on macropore structure of fiber-reinforced clay by industrial computed tomography scanning, in: GeoCalgary 2022, 2022b.

Roustaei, M., Pumple, J., Hendry, M. T., J., Harvey, and Froese, D. (2024) : Effect of freeze–thaw cycles on the macrostructure and failure mechanisms of fiber-reinforced clay using industrial computed tomography, Canadian Geotechnical Journal, 00, 1-15, https://doi.org/10.1139/cgj-2023-0136.

Shur, Y. L.: The upper horizon of permafrost soils, in: Proceedings of the Fifth International Conference on Permafrost, 867–871, 1988.

Soret M, Bacharach SL, Buvat I. Partial-volume effect in PET tumor imaging. J Nucl Med. 2007;48:932–945.

Stephani, E., D. Fortier, Y. Shur, R. Fortier, and G. Doré. "A geosys-tems approach to permafrost investigations for engineering applica-tions, an example from a road stabilization experiment, Beaver Creek,Yukon, Canada."Cold Reg. Sci. Technol.100: 20–35.https://doi.org/10.1016/j.coldregions.2013.12.006, 2014.

Subcommittee, P.: Glossary of permafrost and related ground-ice terms. Associate Committee on Geotechnical Research, National Research Council of Canada, Ottawa, 156, 63-64, 1988. https://doi.org/10.1139/e94-067

Tanaka, E. Y., Yoo, J. H., Rodrigues, A. J., Utiyama, E. M., Birolini, D., and Rasslan, S.: A computerized tomography scan method for calculating the hernia sac and abdominal cavity volume in complex large incisional hernia with loss of domain, Hernia, 14, 63–69, https://doi.org/10.1007/s10029-009-0560-8, 2010.

Torrance, J. K., Elliot, T., Martin, R., and Heck, R. J.: X-ray computed tomography of frozen soil, Cold Reg. Sci. Technol., 53, 75–82, https://doi.org/10.1016/j.coldregions.2007.04.010, 2008.

Wang, S., Yang, P., and Yang, Z. (Joey): Characterization of freeze–thaw effects within clay by 3D X-ray Computed Tomography, Cold Reg. Sci. Technol., 148, 13–21, https://doi.org/10.1016/j.coldregions.2018.01.001, 2018.

Wang, Y., Chen, Z., and Wang, G.: Material segmentation in industrial X-ray CT images using histogram-based thresholding: challenges with unimodal and multimodal distributions, Acta Radiol., 65, 901–911, https://doi.org/10.1177/02841851231225418, 2024.

Wellington, S.L., Vinegar, H.J.: X-ray computerized tomography. J. Pet. Technol. 39 (8), 885–898,1987.

Westermann, S., Langer, M., Boike, J., Heikenfeld, M., Peter, M., Etzelmüller, B., and Krinner, G.: Simulating the thermal regime and thaw processes of ice-rich permafrost ground with the land-surface model CryoGrid 3, Geosci. Model Dev., 9, 523–546, https://doi.org/10.5194/gmd-9-523-2016, 2016.

Zhang, T., Barry, R. G., Knowles, K., Heginbottom, J. A., and Brown, J.: Statistics and characteristics of permafrost and ground-ice distribution in the Northern Hemisphere 1, Polar Geogr., 23, 132–154, https://doi.org/10.1080/10889379909377670, 1999.

Table 1: Sampling location and physical properties of cores analyzed in the study.

Core ID	Length (cm)	Classification/ Properties	Collection Location/ Depositional Environment	Clay (%)	Silt (%)	Sand (%)
BH18-211	23	Ice-rich silt	Alaska HWY, Southwestern Yukon, Canada	11	66	23
BH12F-138	16	ice-rich silty peat (top) and ice-poor silt (bottom)	Alaska HWY, Southwestern Yukon, Canada	top 8 bottom 12	top 52 bottom 57	top 40 bottom 31
BS19-3-6	19	Diamicton	Dempster HWY, Central Yukon, Canada	18	51	31
BH20B-337	20	Ice-poor silt	Alaska HWY, Southwestern Yukon, Canada	8	67	25
DH13-589	26	Ice-rich homogenous peat.	Dempster HWY, Central Yukon, Canada	N/A	N/A	N/A

548

549

550
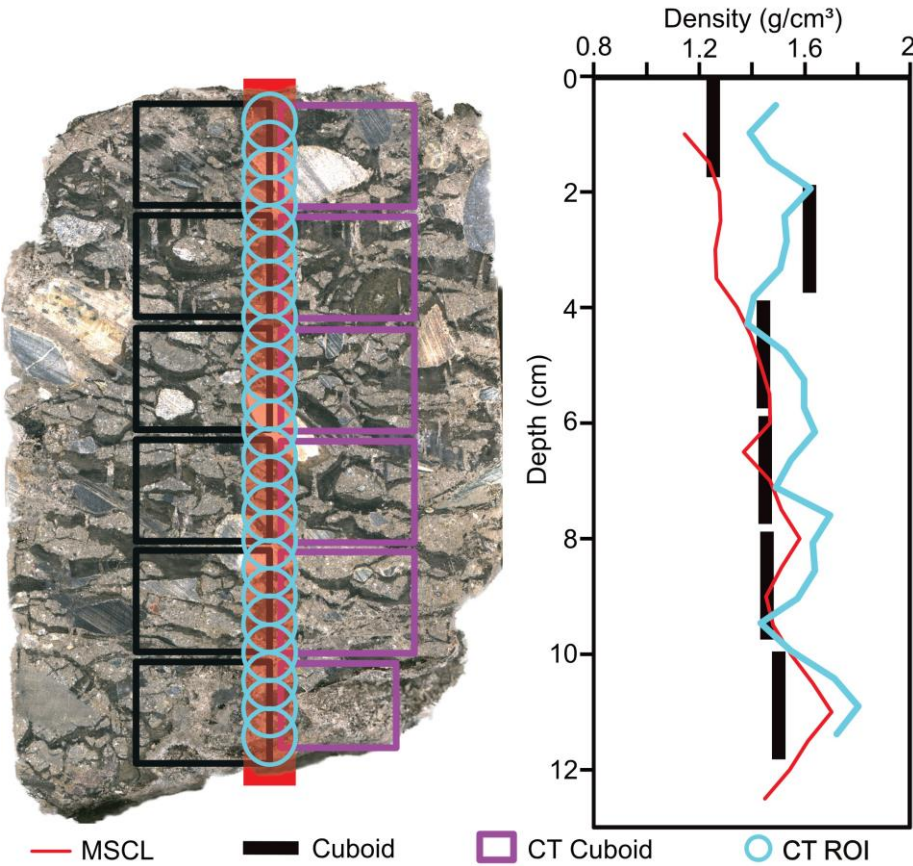
Figure 1: Image of a core highlighting the destructive subsample locations relative to the non-destructive data collection transects (black: subsampled cubes for destructive measurements, purple: subsampled cubes for CT scans)

Figure 2: (A) The CT scanner of the PACS Lab.(B) The internal setup for the core scan. (C) X-ray image of the internal setup of the core (D) X-ray image of the internal setup of the cube.

560

561
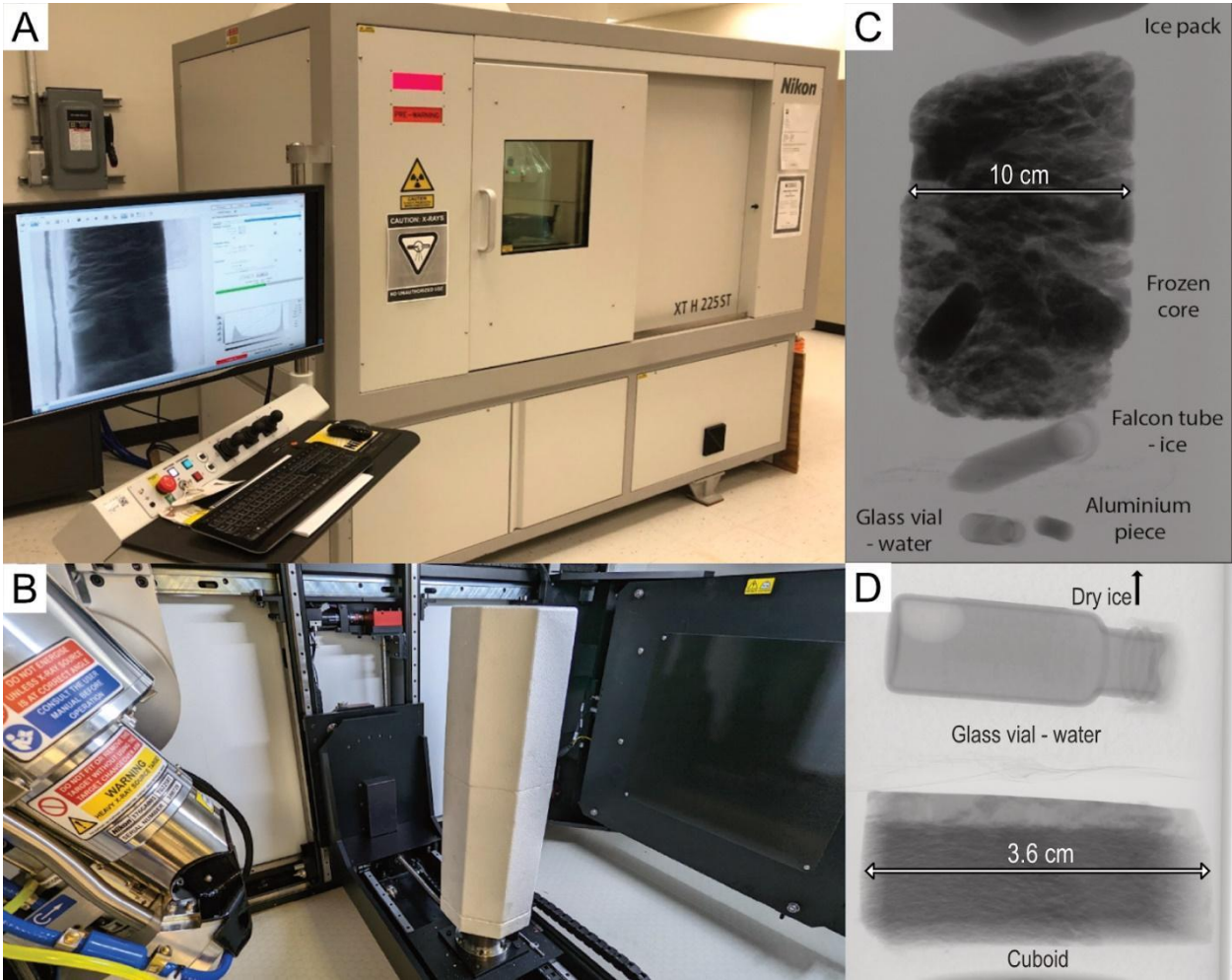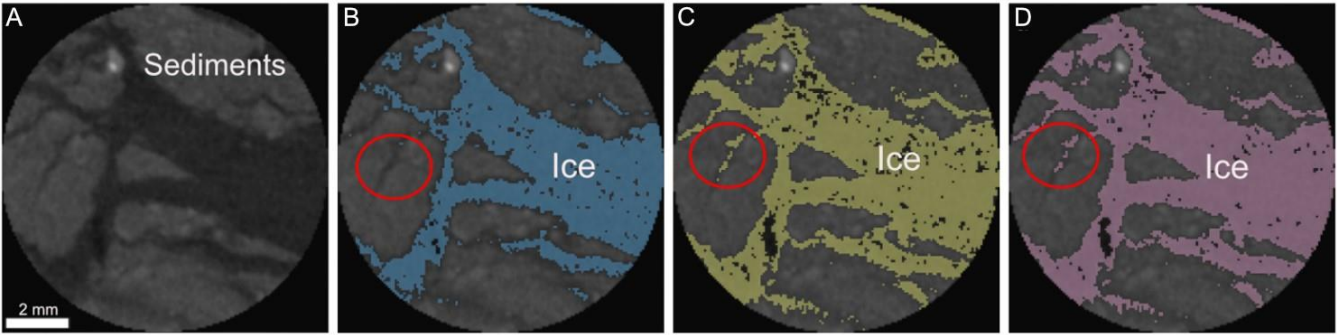
562 **Figure 3: Overview of a slice from ice rich silt core (A) before image processing (B) after the first step, (C) after the second step, and**
563 **(D) after the third step of image processing using the Otsu method.**

564

565
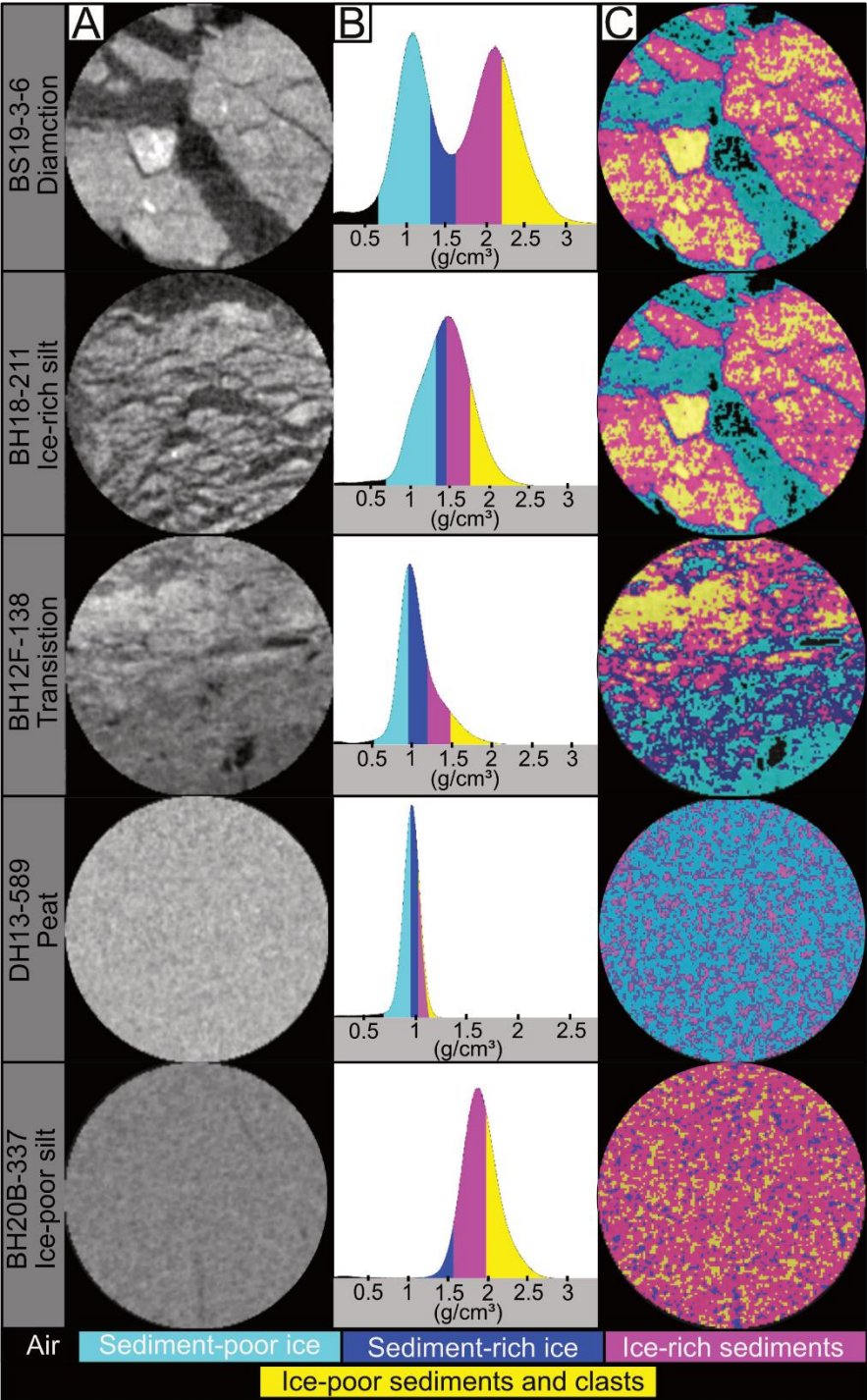
566 **Figure 4: (A) overview of slices from the permafrost cores before image processing (B) histograms, and (C) image segmentation**
567 **results**
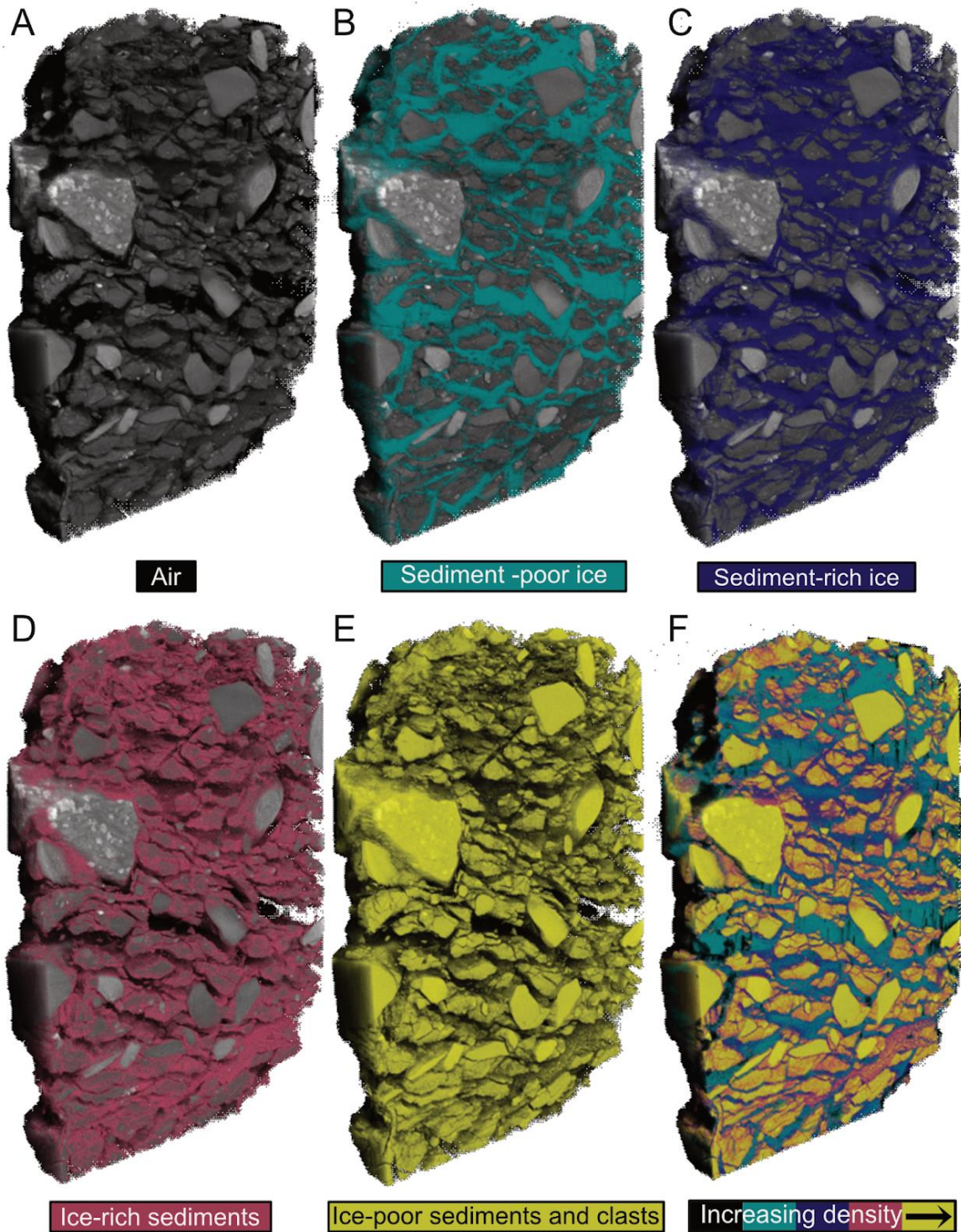
568
569 **Figure 5: Image segmentation results of the diamicton core.**

Table 2: Root mean square error results for the comparison between the CT, Cuboid and MSCL VIC, EIC and density results.

Core ID	RMSE Density CT vs Cuboid (g/cm^3)	RMSE VIC CT vs Cuboid (%)	RMSE VEIC CT vs Cuboid (%)	RMSE Density CT vs Geotek (g/cm^3)	RMSE VIC CT vs Geotek (%)
BS19-3-6	0.14	3	8	0.14	4
BH18-211	0.12	7	9	0.05	8
DH13-589	0.05	1	4	0.03	4
BH12F-138 (top)	0.07	3	7	0.02	11
BH12F-138 (bottom)	0.19	3	2	0.10	10
BH12F-138 (whole core)	0.13	3	5	0.06	10
BH20B-337	0.14	3	5	0.14	3
Overall average	0.12	3	6	0.08	7

571
572
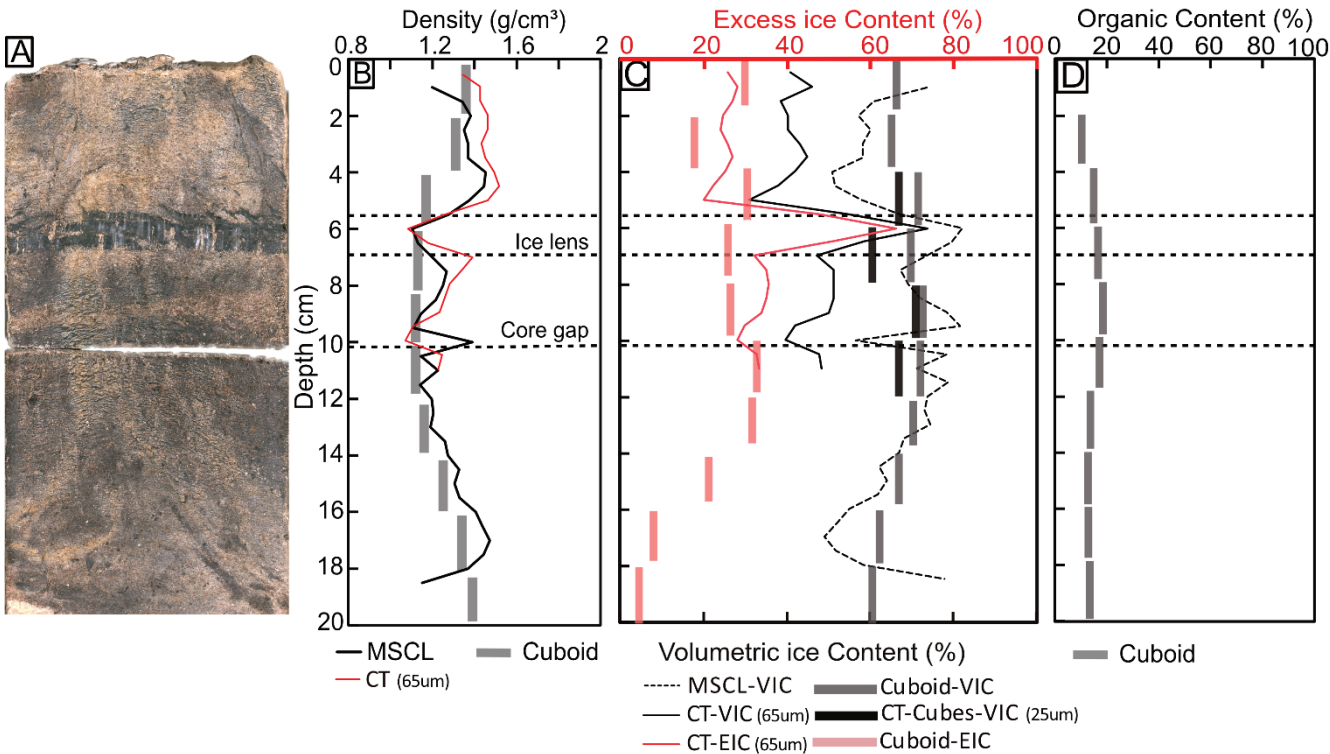
573
574 **Figure 6: (A) MSCL image of the ice-rich, organic-rich silt core; (B) bulk density; (C) ice contents; (D) organic content distribution**
575 **in core depth; (E) black and white image of MSCL image with ice highlighted in black.**

576
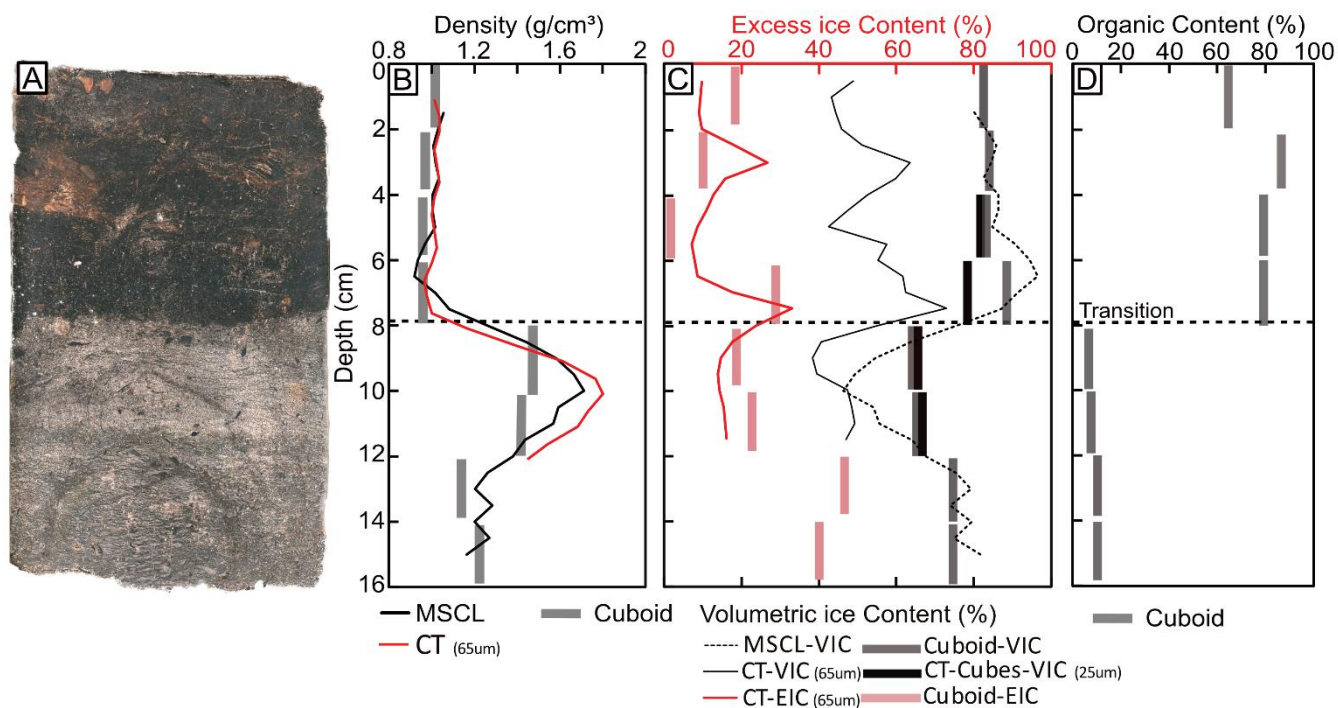
Figure 7: (A) MSCL image of the transition core; (B) bulk density; (C) ice contents; (D) organic content distribution in core depth;
(E) black and white image of MSCL image with ice highlighted in black.

579

580
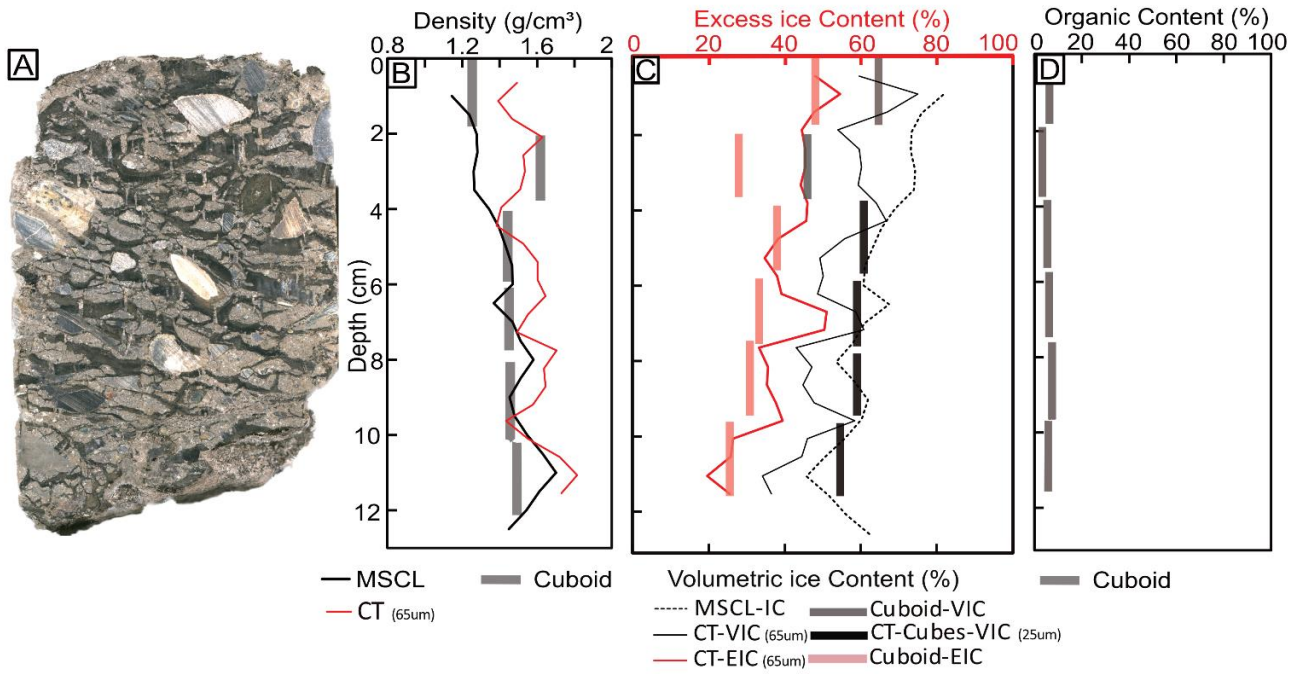
Figure 8: (A) MSCL image of the diamicton core; (B) bulk density; (C) ice contents; (D) organic content distribution in core depth; (E) black and white image of MSCL image with ice highlighted in black.

583

584
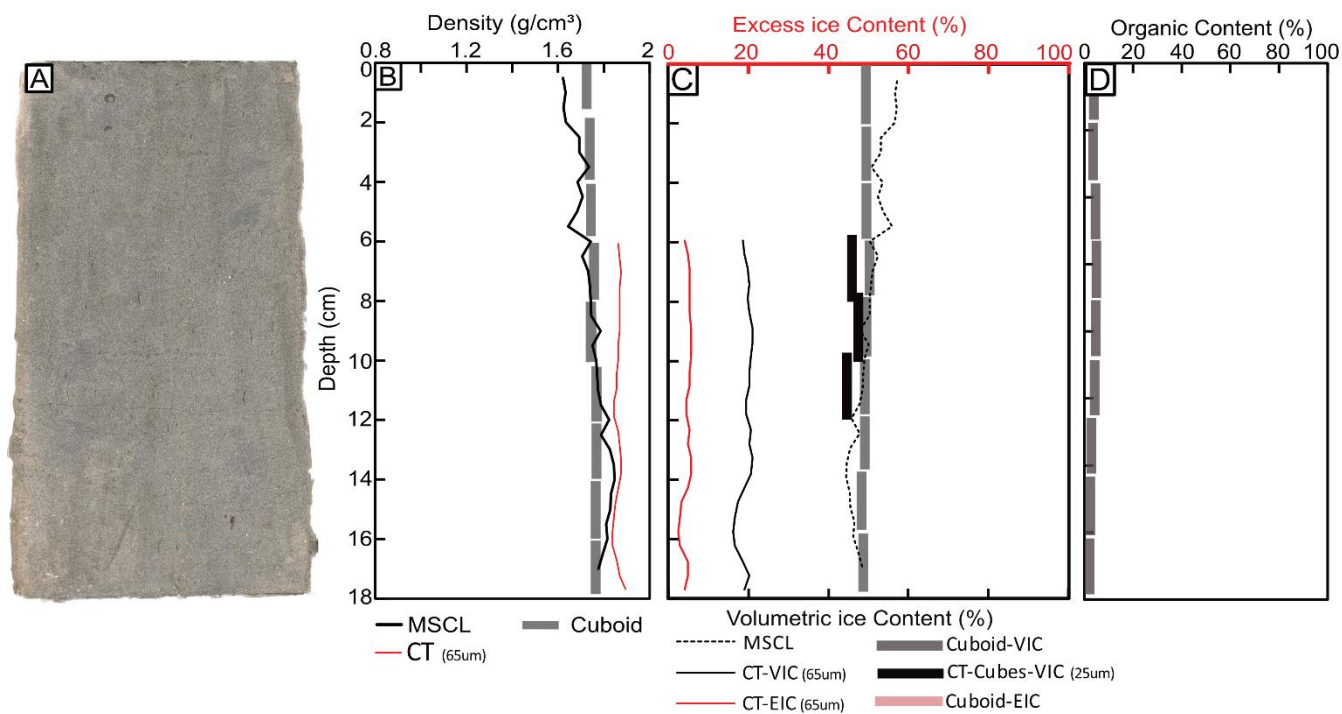
Figure 9: (A) MSCL image of the ice-poor silt core; (B) bulk density; (C) ice contents; (D) organic content distribution in core depth; (E) black and white image of MSCL image with ice highlighted in black.

588
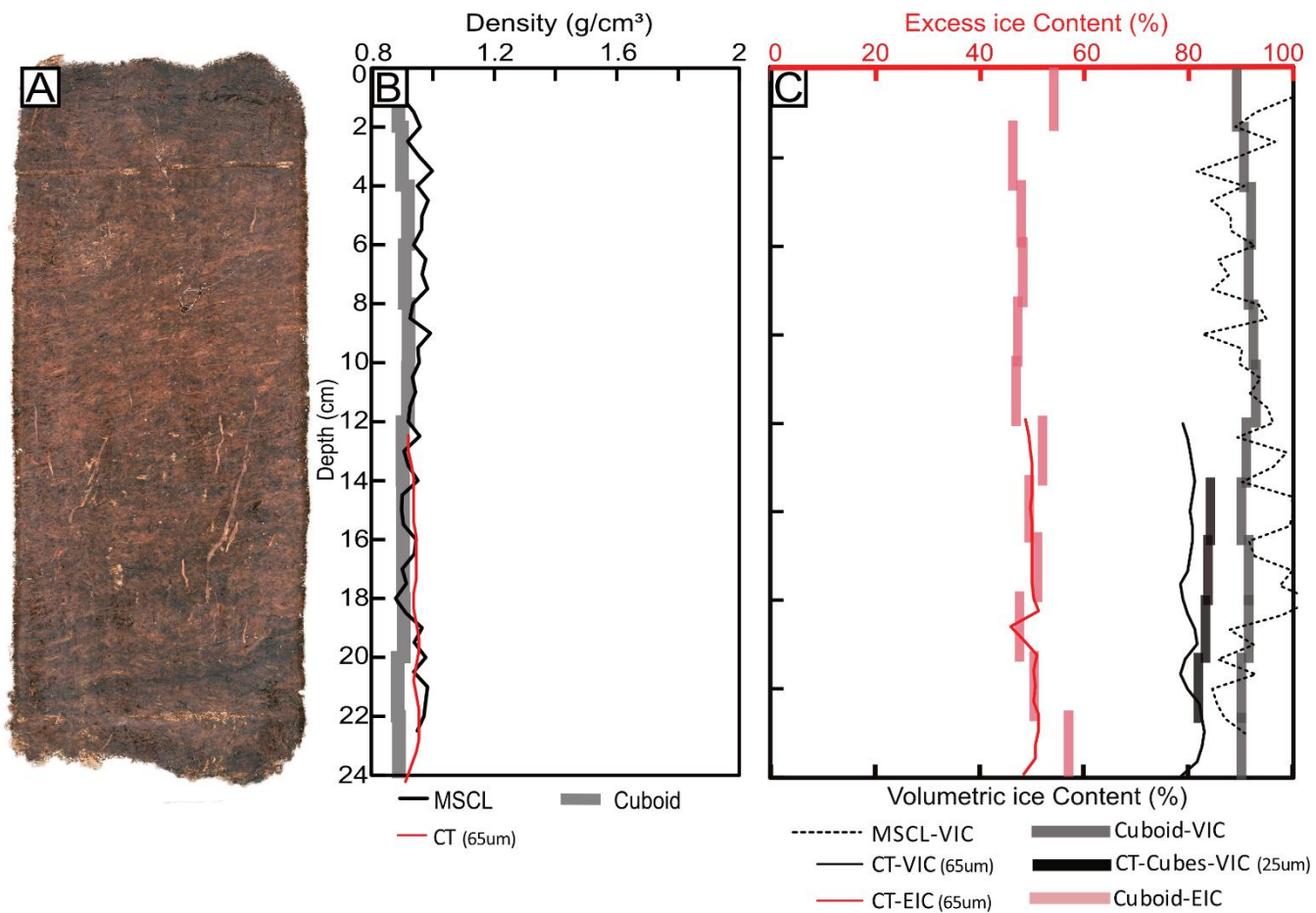
Figure 10: (A) MSCL image of the peat core; (B) bulk density; (C) ice contents; (D) organic content distribution in core depth; (E) black and white image of MSCL image with ice highlighted in black.
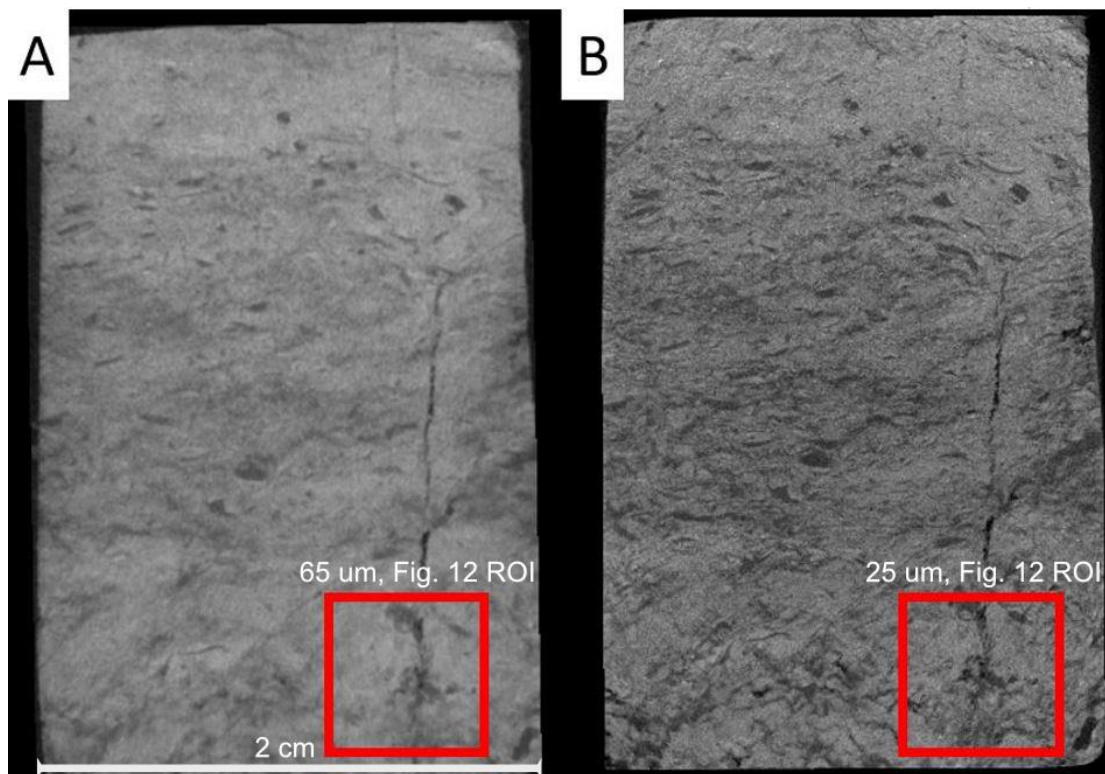
591
592   **Figure 11: CT images of a cube (BH12F-138-10-12 cm) from the transition core at 65 µm (A) and 25 µm (B).**
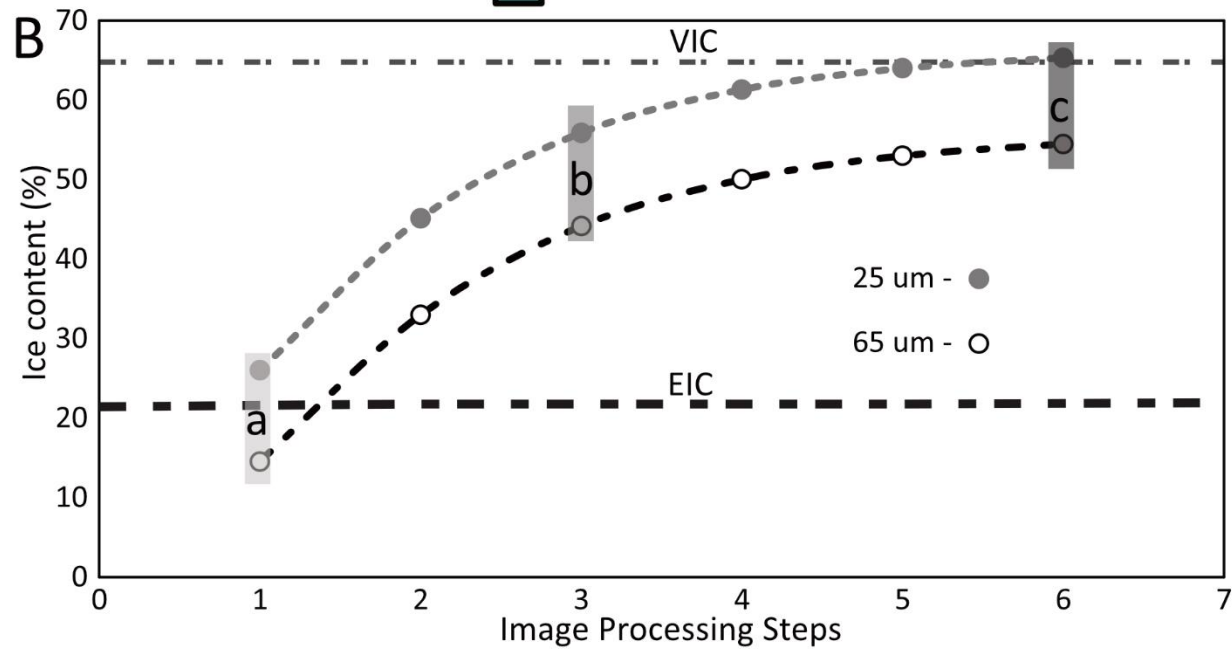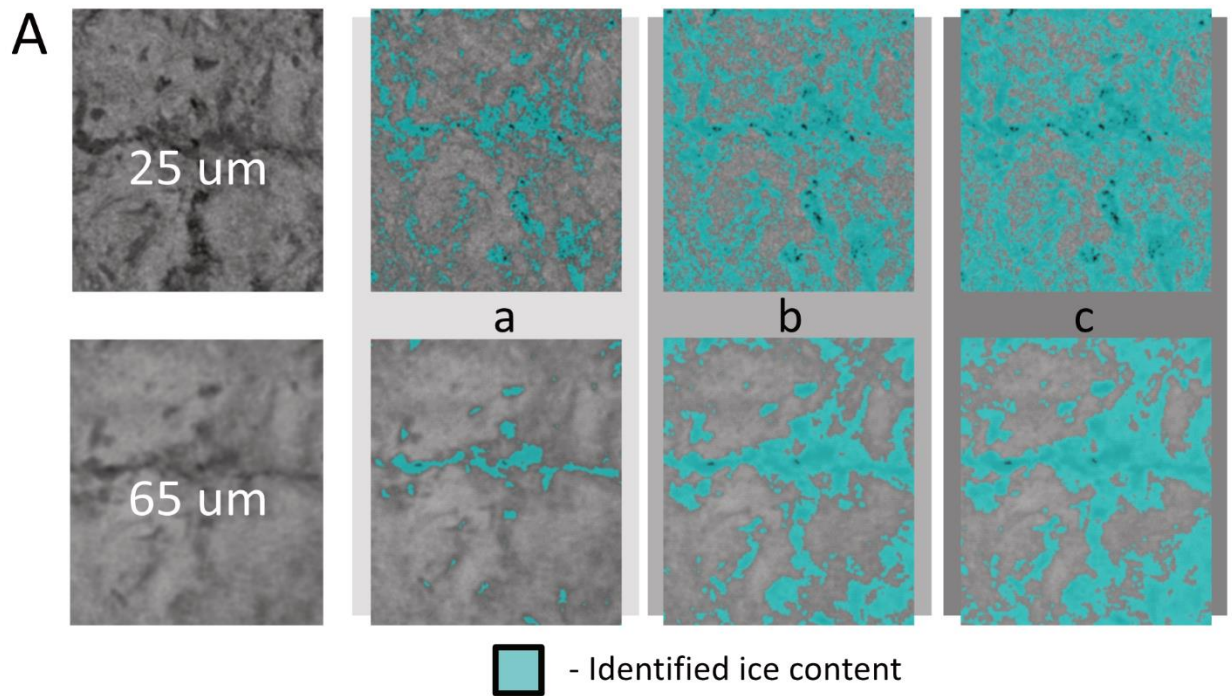
Figure 12: (A) CT ROI's taken from the 65 μm and 25 μm cube scans (BH12F-138-10-12 cm), (B) Identified ice contents at each image processing step using the Otsu split method.

597
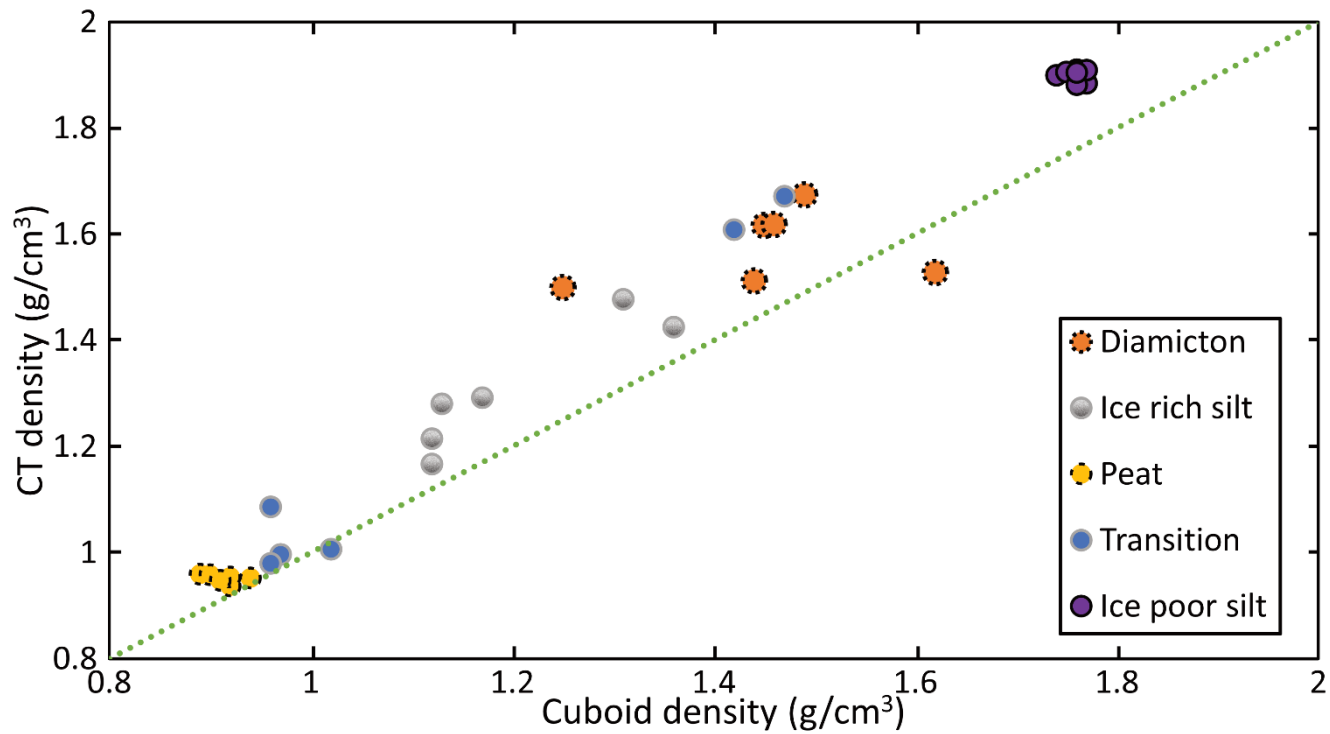
Figure 13: Estimated densities from CT image processing of 65 μm scans vs calculated ones from cuboid method.

599
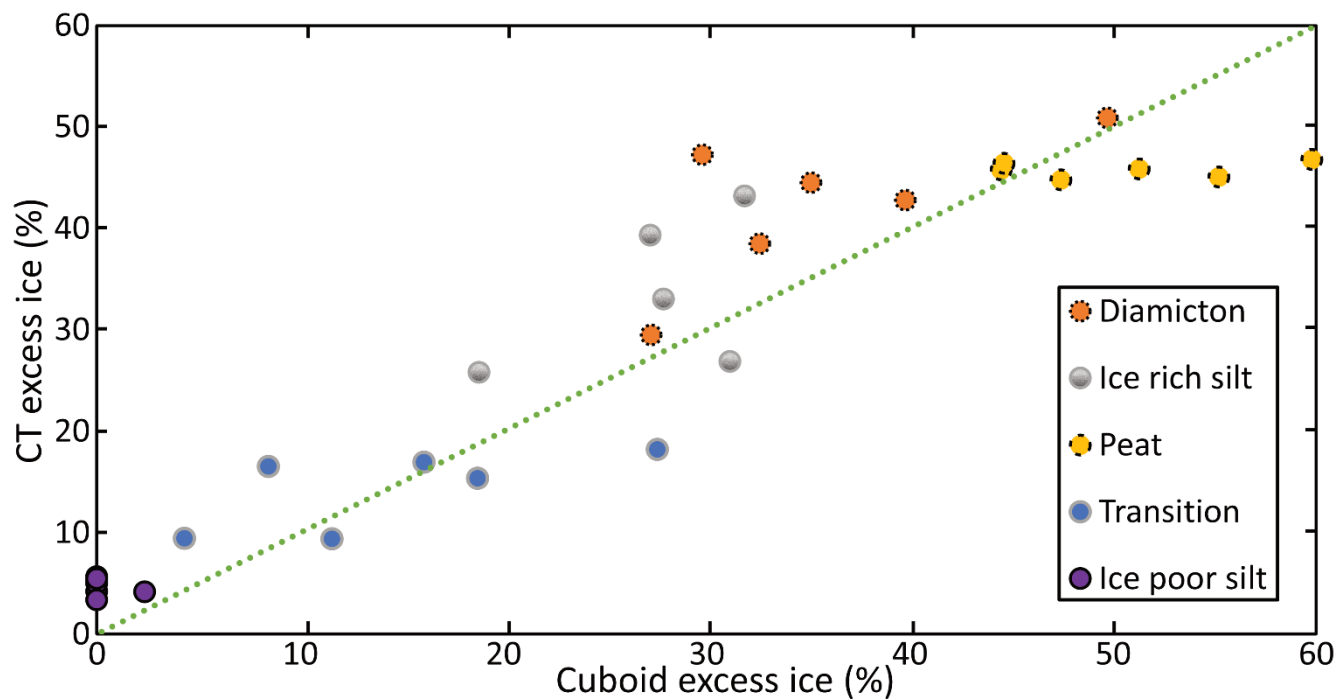
600
601 **Figure 14: Estimated excess ice contents from CT image processing of 65 μm scans vs calculated values from cuboid method.**

602
603 **Figure 15: Estimated volumetric ice contents from CT image processing of 65 μm scans vs calculated values from cuboid method.**
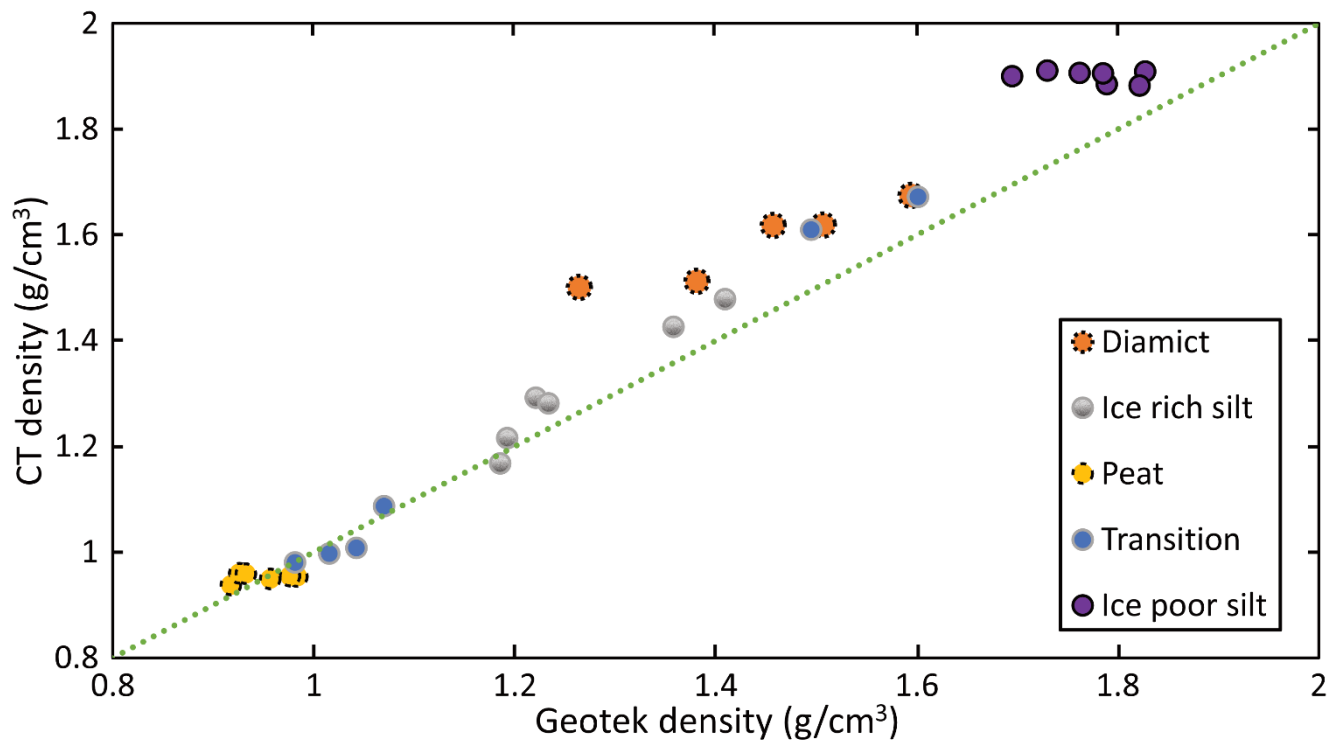
604
605 **Figure 16: Estimated bulk density from CT image processing vs calculated values from MSCL method.**

606
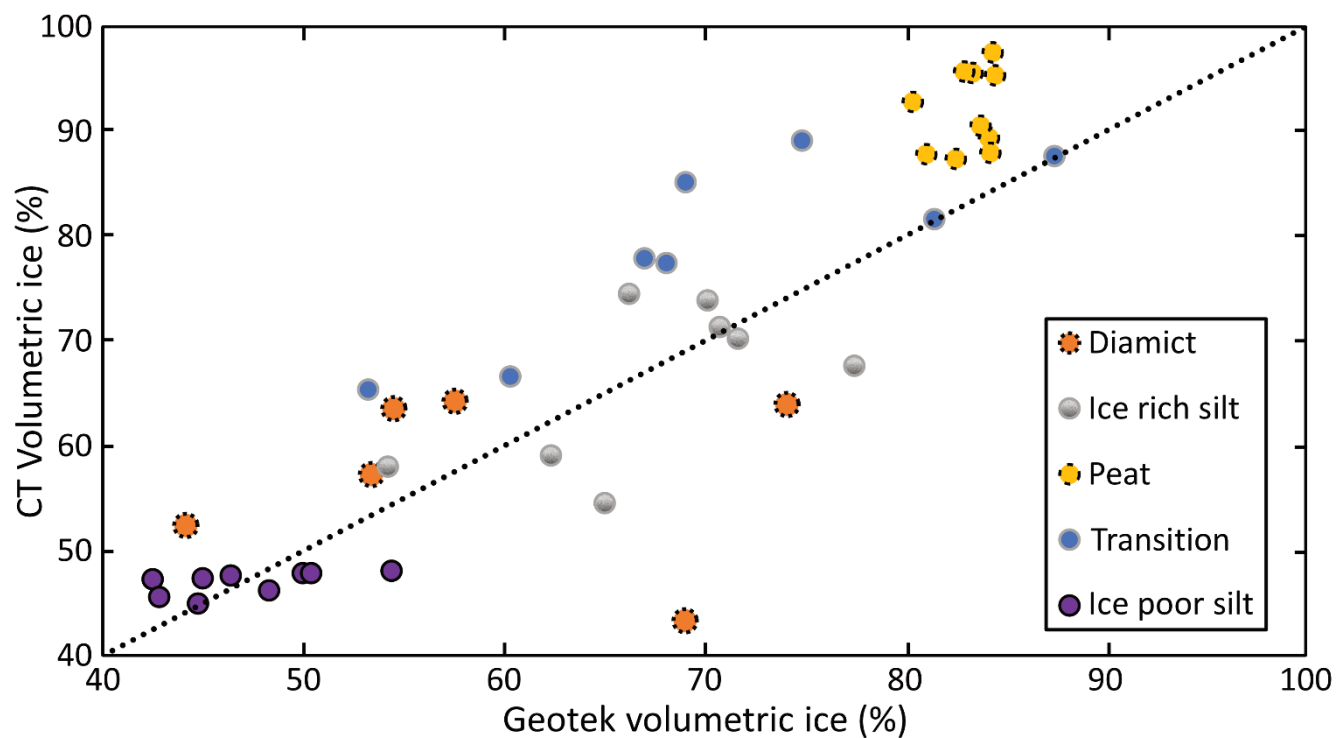
607 **Figure 17: Estimated volumetric ice contents from CT image processing vs calculated values from MSCL method.**

608